Structure development in amorphous Al–La alloys

2003 J. Phys.: Condens. Matter 15 385

(http://iopscience.iop.org/0953-8984/15/3/306)

INSTITUTE OF PHYSICS PUBLISHING JOURNAL OF PHYSICS: CONDENSED MATTER

J. Phys.: Condens. Matter **15** (2003) 385–413 PII: S0953-8984(03)52097-5

Structure development in amorphous Al–La alloys

U Schmidt[1,3], Ch Eisenschmidt[1], F Syrowatka[1], R Bartusch[1], C Y Zahra[2] and A-M Zahra[2]

[1] Martin-Luther-University, Department of Physics, Hoher Weg 8, 06120 Halle, Germany
[2] TECSEN, CNRS-Faculty of Science, 13397 Marseille Cedex 20, France

E-mail: schmidt@physik.uni-halle.de

Received 7 August 2002
Published 13 January 2003
Online at stacks.iop.org/JPhysCM/15/385

Abstract

Melt-spun Al alloys containing 2.7–10 at.% La were studied by means of x-ray diffraction, transmission electron microscopy, electrical resistivity, thermal and microhardness measurements. Fully amorphous structures were only obtained for thin $AlLa_{7.7}$ and $AlLa_{10}$ ribbons and exhibit concentration fluctuations. Phase separation into two metastable bcc structures is observed; they appear successively and are finally replaced by the equilibrium phases α(fcc)Al and (orthorhombic)$Al_{11}La_3$. The transformation kinetics is analysed in terms of a general Johnson–Mehl–Avrami–Kolmogorov model and of local kinetic parameters. The Avrami exponent monitors changes in the crystallization behaviour; nucleation of the stable phases occurs after partial dissolution of the metastable phases. The low values of the activation energy reflect the high instability of these glasses.

1. Introduction

Metals and alloys can be obtained in nonequilibrium including amorphous states by rapid solidification processes [1]. Their stability and transition behaviours depend strongly on the inner electronic structure of the alloys. Amorphous materials based on Al are known to form readily with lanthanides (Ln) and transition metals (T) and have a remarkable stability at room temperature (RT). Yet insufficient information exists about the structure of the amorphous phase, the transition from the amorphous to the crystalline state and the final transformation to the stable crystalline structures.

This contribution presents an investigation of Al–La alloys that adopt different states depending on the La content when rapidly quenched by melt-spinning at different cooling rates deduced from the ribbon thickness obtained. According to Inoue *et al* [2–4], crystalline solid solutions corresponding to α(fcc)Al form up to 7 at.% La. For concentrations between 7 and 10 at.% an amorphous phase appears. At even higher concentrations, the equilibrium phase

[3] Author to whom any correspondence should be addressed.

$Al_{11}La_3$ co-exists first with an amorphous phase, then with α(fcc)Al (>11 at.% La). Recent investigations did not yield the same results, as alloys containing 0.2–4.2 at.% La examined by Dill *et al* [5] were found to consist of α-Al and $Al_{11}La_3$ after melt-spinning. Guo *et al* [6] detected a metastable bcc phase of high hardness as a primary crystalline phase during the decomposition of a fully amorphous Al–8 at.% La alloy.

Small angle x-ray scattering (SAXS) results [7] showed new features that called for a more exhaustive study combining a variety of experimental techniques: transmission electron microscopy (TEM), x-ray diffraction (XRD), calorimetry, electrical resistivity (ER) and microhardness (μHV) measurements.

In section 3.1, the different structures present in the as-quenched states of the investigated materials are characterized by TEM and XRD. In section 3.2, the experimental results of continuous heating experiments from RT up to 600 °C are summarized. Especially the differential scanning calorimetry (DSC) curves and the behaviour of the temperature coefficient of the electrical resistance (TCR) give a complete overview of the structure development in the investigated materials when combined with XRD analyses after heating up to different temperatures. The determination of kinetic parameters from experiments at constant heating rates which have the advantage of shorter experimental times presuppose, however, their temperature independence in a larger temperature region. Investigations of other amorphous Al-rich materials showed that this condition is not fulfilled *a priori*. Therefore isothermal investigations based on ER, calorimetry, XRD and TEM will be presented in section 3.3. In addition to a better apprehension of relaxation phenomena and their influence on the crystallization process, the isothermal studies have the advantage that the structure transitions at chosen temperatures (ϑ_{ISO}) can be pursued over long time intervals, which makes possible a refined modelling described in section 4. The progress of transformation can be evaluated from the intensity of characteristic diffraction peaks as well as from ER and calorimetric measurements. The investigation of other amorphous Al-rich materials has shown that the formation of new phases is controlled by nucleation and growth but cannot be described by the classical Johnson–Mehl–Avrami–Kolmogorov (JMAK) model [8]. Therefore other modelling procedures will be chosen, a more general JMAK model [9] and the concept of a local kinetic parameter [10]. These two possibilities have already been applied successfully to the description of amorphous to crystalline transformations in other AlLnT amorphous ribbons [11, 12].

In the past, only mean activation energies were determined, derived for instance with the help of the Kissinger method [13] or the JMAK equation [14]. It is very unlikely that the activation energy remains constant since transitions from the amorphous to the crystalline structure are very complex in rapidly quenched materials. Hence the determination of a sort of local activation energy will be attempted.

2. Experimental methods

2.1. The production of the ribbons

Al–La alloys with La concentration of 2.7, 5.5, 7.7 and 10 at.% were prepared from the ingot materials 6 N Al and 3 N La by induction melting under argon atmosphere. The ingots were transformed into ribbons using a single-roller melt-spinning plant at different speeds of the copper wheel. The maximum cooling rate on the substrate side was 5×10^5 K s^{-1}. In table 1, the specific electrical resistance, ρ, the density, ρ_D, and the μHV values of the as-quenched states are given together with the mean ribbon thickness, d, which is inversely proportional to the cooling rate. In the case of the presence of crystalline states, the densities of the as-quenched states are indicated.

Table 1. Characteristic mean values of the $AlLa_x$ ribbons. d, mean ribbon thickness of all ER measurements; $\rho_{am.}$, mean specific electrical resistance of the amorphous as-quenched state; $\rho_{cry.}$, mean specific electrical resistance of the crystalline state; $\rho_{Dam.}$, density of the amorphous as-quenched state; $\rho_{Dcry.}$, density of the crystalline state; μHV, microhardness of the as-quenched state (measured on the substrate side).

Alloy (at.%)	d (μm)	Structure of the as-quenched state	$\rho_{am.}$ ($\mu\Omega$ cm)	$\rho_{cry.}$ ($\mu\Omega$ cm)	$\rho_{Dam.}$ (g cm^{-3})	$\rho_{Dcry.}$ (g cm^{-3})	μHV (10 pound)
Error	±15% [a]		±10% [a]	±10% [a]	±3% [b]	±3% [b]	±7% [a]
$AlLa_{2.7}$	28	Crystalline		17[c]		2.94[c]	88
$AlLa_{5.5}$	19	Partly amorphous		134[c]		2.85[c]	265
$AlLa_{5.5}$	68	Crystalline		22[c]		2.96[c]	132
$AlLa_{7.7}$	28	Amorphous	134.5[c]	8[d]	3.17[c]	3.47[d]	168
$AlLa_{7.7}$	49	Partly amorphous	39.9[c]	6[d]	3.15[c]	3.57[d]	122
$AlLa_{7.7}$	69	Crystalline		6[c]		4.17[c]	89
$AlLa_{10}$	29	Amorphous	163.9[c]	8[d]	3.33[c]	3.53[d]	170

[a] Error of the standard deviation.
[b] Error propagation.
[c] Start value.
[d] Final value after heating to 600 °C.

2.2. The experimental methods

In order to assess the quality of the ribbons and their thickness, an incident light microscope was used. The structure and its evolution were examined by TEM using a TESLA 540 instrument ($U = 120$ kV). A scanning transmission electron microscope (STEM), HB 501 ($U = 100$ kV), enabled us to determine also the element distribution after different ageing regimes by energy dispersive x-ray spectroscopy (EDX). The diffraction pattern development (lattice parameter and crystalline structure) was studied with an x-ray diffractometer (D5000, Cu Kα radiation) in the interval of 2Θ between 10° and 70°. To ensure that there was no contribution of crystalline parts when using transmission methods for the investigation of the amorphous structure, the sample surfaces were removed by chemical or ion beam etching at the temperature of liquid nitrogen. Information on the transformation kinetics was obtained from calorimetric measurements with a Perkin–Elmer DSC apparatus and from electrical resistance measurements with a four-point device including a digital voltmeter and interface coupling. The temperature coefficient of the specific ER was calculated according to $\mathrm{TCR} = (\mathrm{d}\rho/\mathrm{d}T)/\rho_0$, with ρ_0 being the initial value. The evolution of a mechanical property was investigated using microhardness measurements on a Bühler tester under 10 pound load. For a more detailed description of all experimental methods, see [11].

3. Experimental results

3.1. The as-quenched state

The state obtained immediately after quenching represents a supersaturated unstable state and an instant image of a highly undercooled melt in the case of the formation of amorphous states. For melt-spun $AlLa_{7.7}$ and $AlLa_{10}$, the as-quenched state was fully amorphous on the substrate side up to a mean ribbon thickness of about 50 μm. The whole ribbon was fully amorphous only for a mean thickness, $d < 30$ μm. At smaller La concentrations, the materials were crystalline, yet in the case of very thin $AlLa_{5.5}$ ribbons ($d < 20$ μm), an amorphous structure formed on the substrate side.

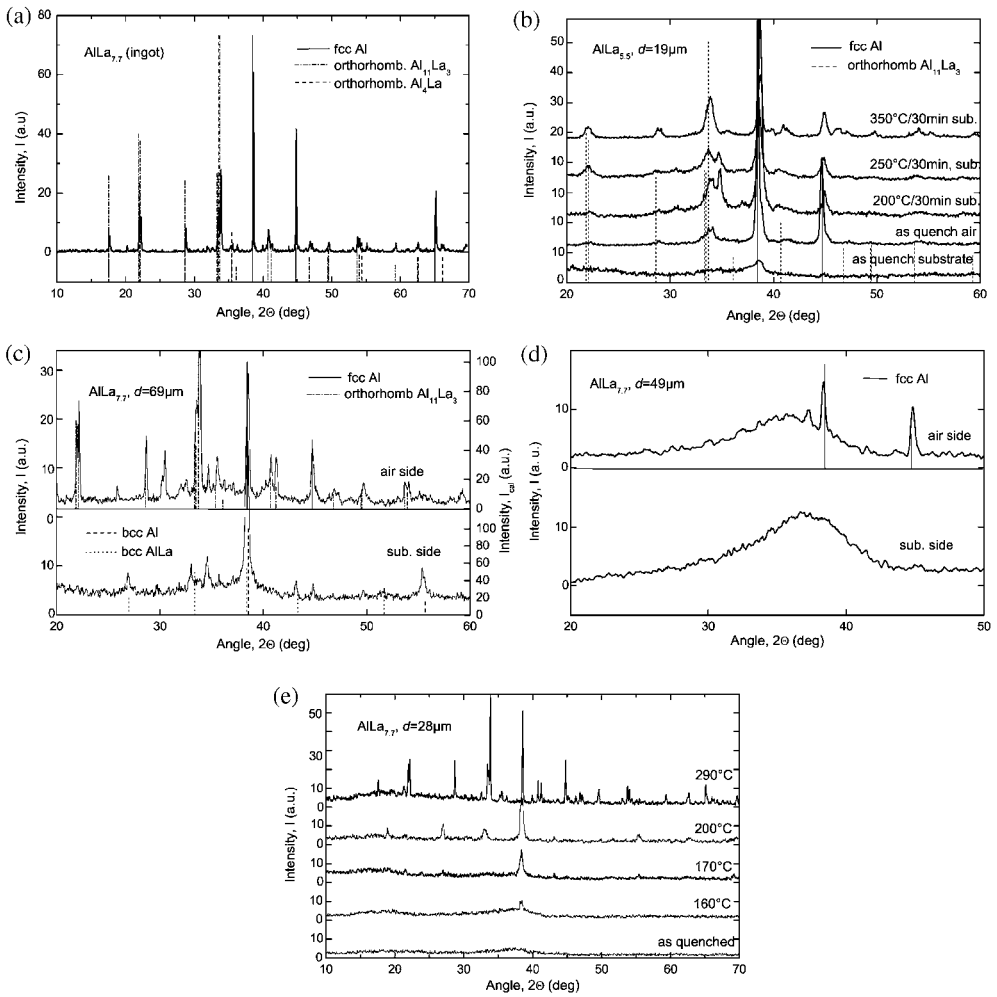

Figure 1. (a) XRD curves of the crystalline $AlLa_{7.7}$ ingot with the structure data of (fcc)Al (solid), (orthorhombic)$Al_{11}La_3$ (dash–dot) and (orthorhombic)Al_4La (dash). (b) XRD curves of the structure of rapidly quenched and annealed $AlLa_{5.5}$ ribbons, $d = 19\ \mu$m; substrate (amorphous) and air (crystalline) cooled sides. (c) XRD curves of the crystalline structure of rapidly quenched $AlLa_{7.7}$ ribbons, $d = 69\ \mu$m substrate (bbc structure) and air (fcc and orthorhombic structures) cooled sides with the structure data of (fcc)Al (solid), (orthorhombic)$Al_{11}La_3$ (dash–dot) and (bcc)Al (dash). (d) XRD curves of the structure of rapidly quenched $AlLa_{7.7}$ ribbons, $d = 49\ \mu$m substrate (amorphous) and air (amorphous + fcc structure) cooled sides. (e) XRD curves of the structure of rapidly quenched $AlLa_{7.7}$ ribbons, $d = 28\ \mu$m, as well as after heating (5 K min^{-1}) to the temperatures indicated.

Figure 1(a) shows the XRD patterns of the crystalline $AlLa_{7.7}$ ingot material from which ribbons were produced by melt spinning. Two phases were found, the α(fcc)Al phase and the α(orthorhombic)$Al_{11}La_3$ phase. Their diffraction patterns according to [15] are included in figure 1(a). It is difficult to distinguish between the α(orthorhombic)$Al_{11}La_3$ and the β(orthorhombic)Al_4La structure of type Al_4Ba which are described in [15, 16], because the diffraction picture is almost the same. In our opinion, the β(orthorhombic)Al_4La phase is formed after quenching and is transformed into α(orthorhombic)$Al_{11}La_3$.

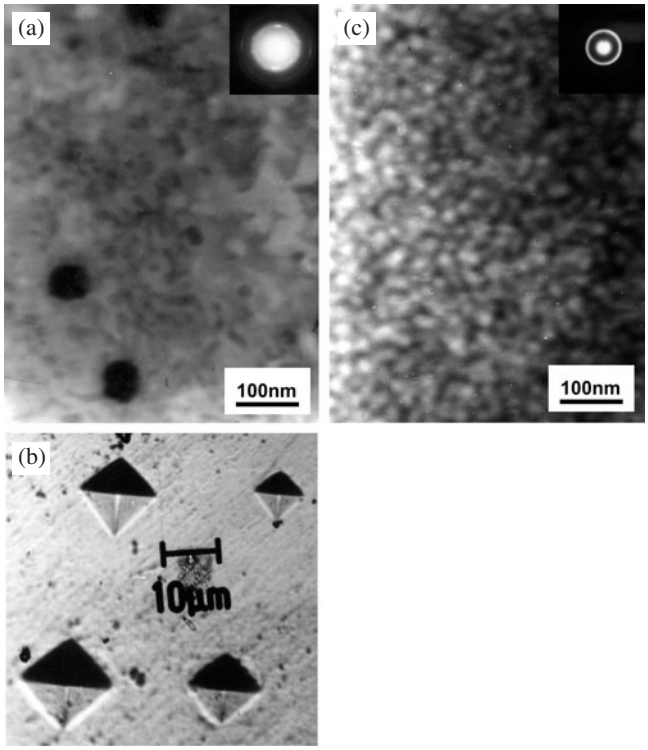

Figure 2. (a) TEM bright field image of $AlLa_{5.5}$ ($d = 68$ nm) in as-quenched state; diffraction ring patterns in inset. (b) LM image of the ribbon cross section of $AlLa_{7.7}$ ($d = 49\ \mu$m) in as-quenched state with μHV indentations (load 10 and 25 pound); amorphous on substrate (top of the figure, $HV = (175 \pm 12)$) and crystalline on air cooled (at the bottom of the figure, $HV = (150 \pm 15)$) sides. (c) TEM bright field image of amorphous $AlLa_{7.7}$ as-quenched state; diffraction ring pattern in inset.

In figures 1(b)–(d), the as-quenched states of the air cooled and substrate sides for $AlLa_{5.5}$ and $AlLa_{7.7}$ cooled at different rates are compared. The as-quenched state of $AlLa_{5.5}$ ($d = 19\ \mu$m) (figure 1(b)) shows on the substrate side an amorphous structure and on the air quenched side the α(fcc)Al phase and small amounts of the $Al_{11}La_3$ phase. After isothermal ageing for 30 min at 200, 250 and 350 °C, the stable structure of (orthorhombic)$Al_{11}La_3$ develops on the substrate side. The broad diffraction peaks indicate the presence of a fine crystalline structure. A TEM observation of an $AlLa_{5.5}$ alloy in the as-quenched state confirms that a finely dispersed structure exists (figure 2(a), bright field image and diffraction pattern in inset), with a grain size of about 100 nm.

The development of different structures in dependence on the cooling rate is illustrated by the XRD pattern of $AlLa_{7.7}$. In figure 1(c), the air cooled side of a ribbon ($d = 69\ \mu$m) shows the (fcc)Al and the (orthorhombic)$Al_{11}La_3$ crystalline structures. The diffraction peaks from the substrate side are different. The structures of the equilibrium phases cannot be identified clearly but a new crystalline structure is present—a metastable (bcc)Al phase—discussed in section 4.1.1.

In figure 1(d), the diffraction patterns of the air cooled and the substrate sides are shown for $AlLa_{7.7}$, $d = 49\ \mu$m (corresponding to a cooling rate of 5×10^4 K s^{-1}). The amorphous diffuse diffraction patterns exist on both sides, but on the air cooled side (fcc)Al crystals are also detected.

In figure 1(e), the diffraction pattern of the fully amorphous $AlLa_{7.7}$ alloy ($d = 28\ \mu m$) in the as-quenched state is shown together with the crystallization patterns obtained after heating to different temperatures (see section 3.2.3).

A light microscopic (LM) image (figure 2(b)) of the amorphous $AlLa_{7.7}$ ($d = 49\ \mu m$) alloy used for figure 1(d) shows the presence of crystalline and amorphous structures over the ribbon cross section, together with hardness indentations. The hardness values of the amorphous and crystalline parts are given under different loads (10 and 25 pound). The partly crystallized regions on the air cooled side do not change their structure during a heat treatment.

A study of the amorphous structure of the melt-spun Al–La alloys containing 7.7 or 10 at.% La by TEM shows different regions, similar to the results described by Guo *et al* [6]. In figure 2(c) which is relative to $AlLa_{7.7}$ ($d = 28\ \mu m$), the diffraction picture of the as-quenched state is included. It corresponds to an amorphous state but exhibits a duplex structure. The measurement of the element distribution by EDX gives the following mean concentrations across the sample in the as-quenched state: $c(Al) = (94.0 \pm 0.9)$ at.% and $c(La) = (6.0 \pm 0.8)$ at.%. However, the La concentration varies across the sample between (3.5 ± 1.0) and (6.3 ± 1.0) at.%, and there are no signs of decomposition for the ratios corresponding to the two possible stable phases ($c(Al)/c(La) = 11/3$ in $Al_{11}La_3$ and nearly pure Al for (fcc)Al). The concentration ratios of Al and La were determined from the relation $c(La)/c(Al) = k_{AlLa} \cdot I_{La}/I_{Al}$. I_{Al} and I_{La} are the measured intensities of the Kα radiation of the Al and La elements; k_{AlLa} is the device factor determined from integral measurements.

3.2. Decomposition during continuous heating

3.2.1. DSC measurements. Figure 3 shows the exothermal heat effects normalized to the heating rate (specific heats changes) which accompany the transition from the amorphous to the stable crystalline state in the case of an $AlLa_{7.7}$ alloy heated at 20 (full curve) or 1 K min^{-1} (discontinuous curve). The specific heat accompanying the first crystallization process (having a peak temperature of 179 °C at a heating rate of 20 K min^{-1}) is of -18 J g^{-1}, whereas the following two overlapping effects yield -53 J g^{-1} (about -40 J g^{-1} at 1 K min^{-1} with different integration conditions); the strongest peak lies at 268 °C. Guo *et al* [6] found about the same heat values but higher peak temperatures (200 °C, respectively 277 °C). The reason for these discrepancies is probably due to different fabrication conditions and different storage times at RT before the analysis, leading to different numbers of nuclei. Rubshtein *et al* [17] observed (without giving values) that the temperature values of the exothermal peaks during heating amorphous $AlLa_9$ alloys depend on the melt temperature. Similar DSC curves are obtained during the heating of amorphous $AlLa_{10}$ ribbons, but precipitation starts a bit later than in $AlLa_{7.7}$.

3.2.2. ER measurements. Around 175 °C, the ER changes strongly too during heating amorphous $AlLa_{7.7}$ and $AlLa_{10}$ at 5 K min^{-1} (figure 4(a)). In contrast to the DSC results, the first transformation is accompanied by a double peak in the TCR curve (inset of figure 4(a)). During the heating with smaller rates (2 K min^{-1} for $AlLa_{7.7}$, see figure 4(a)), crystallization begins earlier and the transformation interval is broader. The double peak accompanies the formation of two different metastable (bcc) phases, as will be shown in section 4.1.1. For the remaining Al–La materials (table 1), the heating curves are recorded at a rate of 10 K min^{-1} and the derived TCR values are shown in figure 4(b). In the materials without amorphous parts ($AlLa_{2.7}$, $d = 28\ \mu m$ and $AlLa_{5.5}$, $d = 68\ \mu m$), relaxation and crystallization phenomena are absent. A remarkable change of the TCR sets in for temperatures > 300 °C and is accompanied by the development of a grain structure in LM images. In the presence of certain amounts of amorphous structure ($AlLa_{5.5}$, $d = 19\ \mu m$), the ER changes at temperatures > 170 °C.

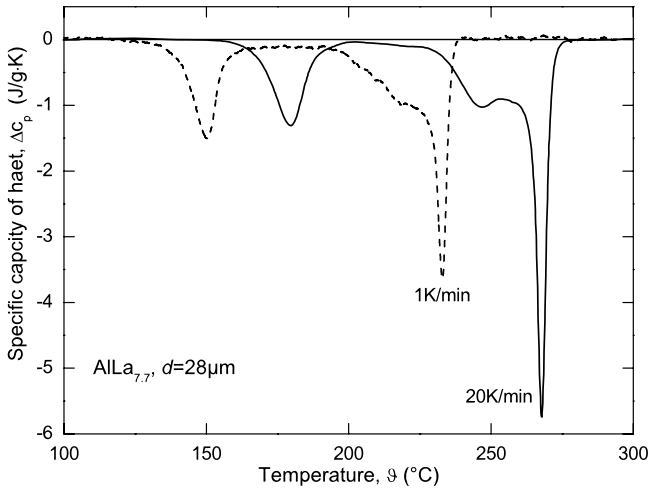

Figure 3. DSC curves of $AlLa_{7.7}$ heated at 20 K min^{-1} (solid) and at 1 K min^{-1} (dash).

This process is not clearly separated from the following transformations. For the $AlLa_{7.7}$ alloy, $d = 69$ μm, already being in the metastable bcc structure in the as-quenched state (cf figure 1(c)), the ER changes strongly at temperatures ≈200 °C; the metastable structure starts to transform into the stable phases.

3.2.3. XRD results. The evolution of the diffraction patterns when heating the amorphous $AlLa_{7.7}$ and $AlLa_{10}$ alloys at 5 K min^{-1} up to different temperatures is included for $AlLa_{7.7}$ in figure 1(e). Heating up to 160 °C shows the first sign of crystallization; a small peak develops at 38.5°. After heating to 170 °C it is possible to detect a crystalline structure which is different from the known (fcc)Al structure. An additional structure forms when heating up to 200 °C, which is not in coincidence with the (orthorhombic)$Al_{11}La_3$ structure. Only after heating to 290 °C can the diffraction peaks be assigned to the (fcc)Al and the (orthorhombic)$Al_{11}La_3$ structures. A calculation and interpretation of the structures of the new phases will be given in section 4.1.1.

A pre-peak begins to appear in the structure factor $S(Q)$ representation [18] already at 160 °C. This pre-peak does not exist in the as-quenched state of freshly prepared materials but begins to develop in naturally aged materials (more than three years). It is known from other investigations (see [3, 19]) that the development of a pre-peak monitors changes in the short-range order (SRO) between the atoms.

3.2.4. Isochronal µHV. The hardness values were measured on different ribbons after the following heat treatments. The samples were aged for 10 min at the temperatures ϑ given in figure 5; the temperature interval between two measurement points is 30 K, beginning at 30 °C and ending at 600 °C; heating between RT and ϑ took less than 5 s. In all materials, amorphous or not amorphous, a small increase in hardness of unknown origin is found up to 100 °C. The increase is due to the annealing of quenched-in defects (spontaneous relaxation), whereas the minimum indicates structural relaxation in the materials. The increased ordering of the atoms in the amorphous state facilitates the motion of the slip bands. A new hardness increase is observed in the region of the transition to the crystalline state or during structure changes of the crystalline as-quenched state. Then the hardness decreases once more, because

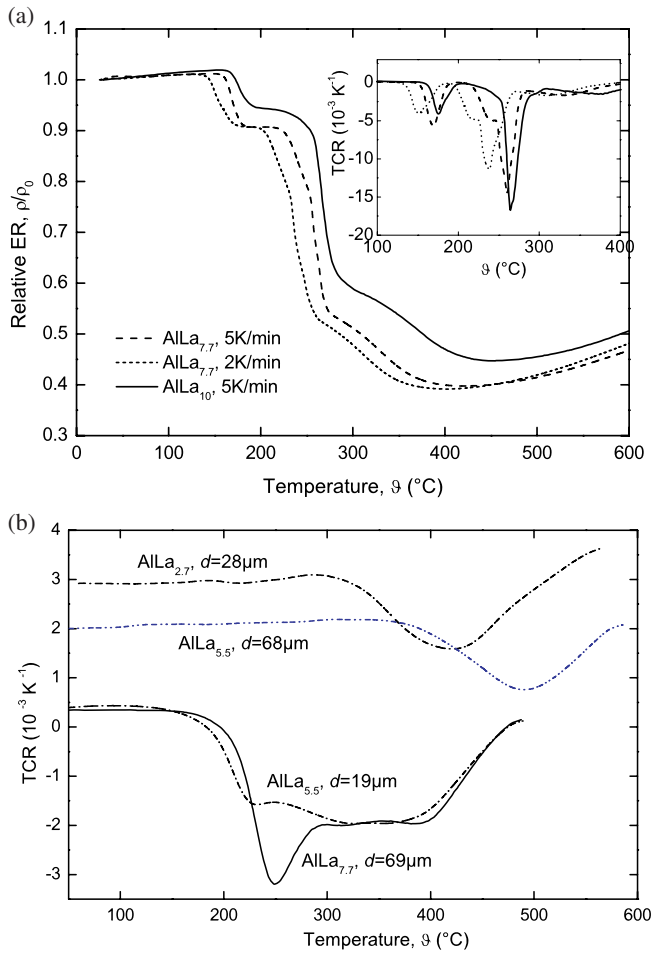

Figure 4. (a) ER heating curves, 2 (dot), 5 K min^{-1} of amorphous $AlLa_{7.7}$ (dash) and $AlLa_{10}$ (solid); in the inset, the TCR curve up to 400 °C (ρ_0, start value at RT). (b) TCR curves (heating rate 10 K min^{-1}) of different $AlLa_x$ ribbons (d, mean thickness).

of the re-crystallization. It has been proposed previously [11, 19] that in amorphous alloys, irreversible relaxation provokes hardness decreases, whereas relaxation leading to better SRO as well as formation of small crystals subsequently increases the hardness.

In $AlLa_{7.7}$, the increase in hardness is due to a reversible relaxation and first crystallization to bcc structures and occurs earlier than in $AlLa_{10}$, being in good agreement with the ER measurements (figure 4(a)); the subsequent formation of stable phases maintains a high hardness level over a long temperature interval. Yet hardness values attained are higher for $AlLa_{10}$ due to more precipitation. Grain coarsening is responsible for the loss of hardness at even higher temperatures. The highest initial μHV values are attained by $AlLa_{5.5}$ ($d = 19\,\mu$m) due to the fine crystalline structure present after melt-spinning (figure 2(a)).

3.3. Isothermal ageing studies

3.3.1. XRD analyses. Ageing of $AlLa_{7.7}$ at 175 °C (figure 6(a)) produces at the beginning (at $t \leqslant 30$ min) the formation of a faint and complex structure, a body centred cubic structure,

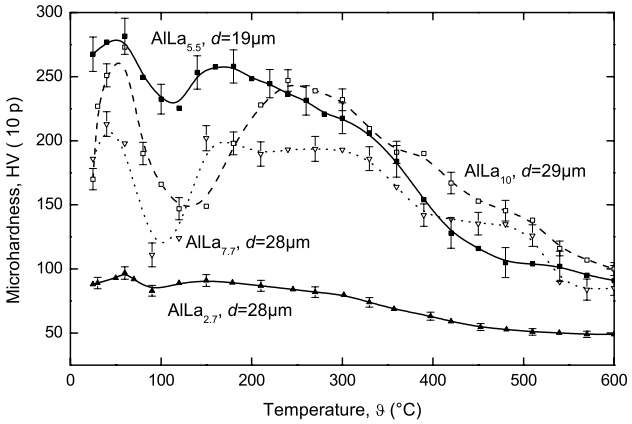

Figure 5. Isochronal μHV evolution (10 min/measurement point) of the different $AlLa_x$ ribbons (d, mean thickness).

named (bcc)Al, in a residual amorphous matrix. At $t = 60$ min, an additional phase also having a bcc structure has developed, named (bcc)AlLa; it must not be confounded with the intermetallic phase AlLa [21]. The nature of these crystalline phases is not identical with known stable phases of the Al–La system. It will be confirmed in section 4.1.1 that the crystalline structures formed from the amorphous state can be identified as bcc structures. Only at ageing times $>$ 30 h does the beginning of the transformation to α(fcc)Al become observable. After 72 h, a mixture of two phases is found (figure 6(a)), α(fcc)Al and (orthorhombic)$Al_{11}La_3$.

The XRD background for $AlLa_{7.7}$ in the as-quenched state shows a partially amorphous structure with irregular, small crystalline regions up to 120 min at 175 °C. The amorphous parts and the small crystals are the reasons for the strong background intensity and the large peak width.

After ageing at temperatures $\geqslant$230 °C, two stable phases, the α(fcc)Al phase and the (orthorhombic)$Al_{11}La_3$ phase co-exist. In figures 6(b) and (c), the changes of the structure after different ageing conditions are illustrated for two very interesting diffraction regions. Figure 6(b) indicates the replacement of the (fcc)Al structure ([111] and [200] peaks) by the (bcc)Al structure ([110] peak). Figure 6(c) shows the change of the (bcc)AlLa phase ([211] peak) into the (orthorhombic)$Al_{11}La_3$ phase ([123] peak).

The crystallization behaviour of the $AlLa_{10}$ amorphous materials (figure 6(d)) does not differ substantially from $AlLa_{7.7}$. At 150 °C/5 min, crystallization begins with the formation of (bcc)Al. At longer ageing times (150 °C/30 min), the (bcc)AlLa structure can be detected. These two phases co-exist for a long time (150 °C/3400 min). At 175 °C, a mixture of bcc structures is also present for long times. At 230 °C/30 min, the (fcc)Al and (orthorhombic)$Al_{11}La_3$ phases can be identified.

3.3.2. TEM observations. Electron microscopic observations on $AlLa_{7.7}$ after ageing at different temperatures (175, 185, 230, 250 and 260 °C) confirm the structure evolution.

Figure 7(a) shows a bright field image obtained by TEM (TESLA 540) together with the diffraction images after ageing at 175 °C/30 min which leads in most cases to a fine disperse structure (region 1). In any region, a structure has been formed with a regular diffraction pattern (region 2 in figure 7(b)). The determination of the lattice constants of the phases will be given in section 4.1. Microdiffraction images with the help of STEM-HB 501 in region 1

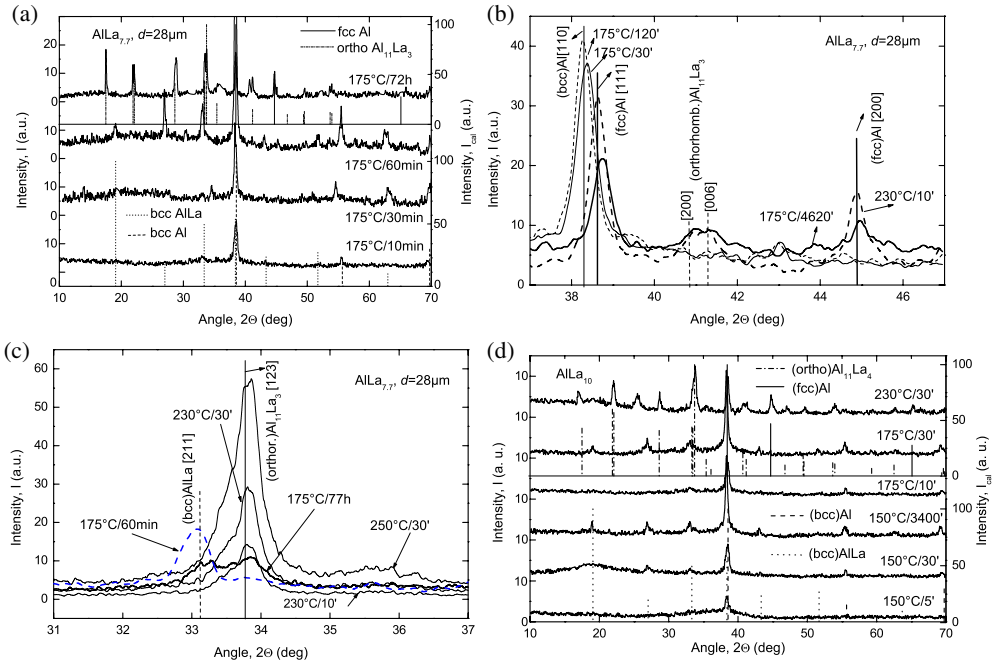

Figure 6. (a) XRD curves of $AlLa_{7.7}$ after isothermal ageing at 175 °C for the times indicated and the structure data of (bcc)Al (dash), (bcc) AlLa (dot), (ortho)$Al_{11}La_3$ (dash–dot) and (fcc)Al (solid). (b) Changes in the diffraction pattern of $AlLa_{7.7}$ accompanying the transition of (bcc)Al [110] into (fcc)Al [111] and [200] during the heat treatments given. (c) Changes in the diffraction pattern of $AlLa_{7.7}$ accompanying the transition of (bcc)AlLa [211] into (orthorhombic)$Al_{11}La_3$ [123] during the heat treatments given. (d) XRD curves of $AlLa_{10}$ after various isothermal heat treatments and the structure data, (bcc)Al (dash), (bcc) AlLa (dot), (ortho)$Al_{11}La_3$ (dash–dot) and (fcc)Al (solid).

(This figure is in colour only in the electronic version)

confirm the formation of finely dispersed crystals in the amorphous matrix (figure 7(c), bright field image, diffraction pattern in inset). The formation of small crystals at 175 °C/30 min begins without any appreciable concentration changes with respect to the as-quenched state, i.e. the concentration profile is nearly the same as in the as-quenched state.

The structure changes between 185 °C/30 min and 230 °C/30 min. A first look at the TEM pictures (figures 8(a) and (b), TESLA 540 TEM) seems to indicate an irregular structure. But the formation of a lamellar structure is observed in different regions (figure 8(c), STEM-HB 501, 230 °C/30 min). The Al and La concentrations are determined at MP1 and MP2.

- MP1: $c(\mathrm{Al}) = (91.1 \pm 0.9)$ at.%; $c(\mathrm{La}) = (8.9 \pm 0.6)$ at.%.
- MP2: $c(\mathrm{Al}) = (96.2 \pm 1.5)$ at.%; $c(\mathrm{La}) = (3.8 \pm 0.6)$ at.%.

The mean concentrations across the sample are $c(\mathrm{Al}) = (93.7 \pm 1.1)$ at.% and $c(\mathrm{La}) = (6.3 \pm 0.6)$ at.%.

The final crystalline structure is obtained after heating at 260 °C for 30 min and more (figure 9(a) (TESLA 540 TEM)), diffraction pattern in inset). The (orthorhombic)$Al_{11}La_3$ phase is finely dispersed in the (fcc)Al matrix. The diffraction pattern confirms the formation of a microstructure in the ribbons. The scanning of the Al and La concentrations in different

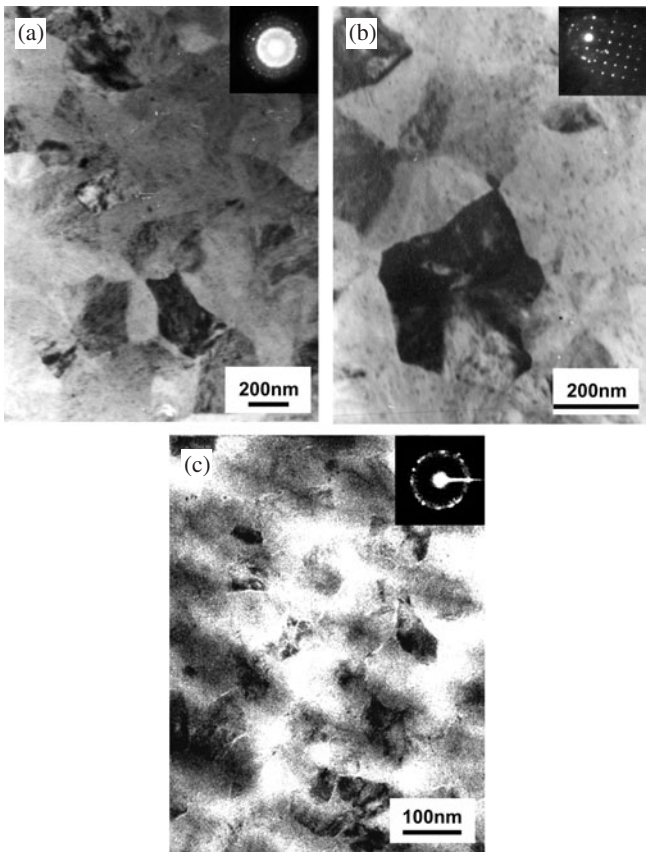

Figure 7. (a) TEM image of $AlLa_{7.7}$ showing the presence of (bcc)Al(La) after 175 °C/30 min (region 1); diffraction ring patterns in inset. (b) TEM image of $AlLa_{7.7}$ after 175 °C/30 min (region 2) showing the formation of (bcc)Al; diffraction pattern [111] orientation in inset. (c) STEM image of $AlLa_{7.7}$ (region 1) after 175 °C/30 min, diffraction ring pattern in inset.

regions (figure 9(b) (260 °C/30 min) and figure 9(c) (250 °C/2 h, see MPi markers)) confirms the different structures.

- MP1: $c(\mathrm{Al}) = (75.1 \pm 1.5)$ at.%; $c(\mathrm{La}) = (24.9 \pm 1.6)$ at.%.
- MP2: $c(\mathrm{Al}) = (99.2 \pm 2.9)$ at.%; $c(\mathrm{La}) = (0.8 \pm 0.6)$ at.%.
- MP3: $c(\mathrm{Al}) = (78.3 \pm 1.3)$ at.%; $c(\mathrm{La}) = (21.7 \pm 1.4)$ at.%.

The mean concentrations across the sample are $c(\mathrm{Al}) = (91.1 \pm 2.0)$ at.% and $c(\mathrm{La}) = (8.9 \pm 1.2)$ at.%.

Longer heating times and/or higher temperatures lead to increases in the dimension of the phases and the brittleness of the ribbons. The fact that the mean La concentration across the samples at 250 °C/2 h and at 260 °C/30 min is higher when using standard free x-ray intensity measurements is due to the sample preparation. Samples for STEM measurements were thinned by ion beam etching which is known to attack preferentially crystalline (fcc)Al in Al materials.

3.3.3. ER studies. As isothermal ER studies have proven to be a very sensitive means for investigating structure development in amorphous alloys [11, 19], the behaviour of the ER is

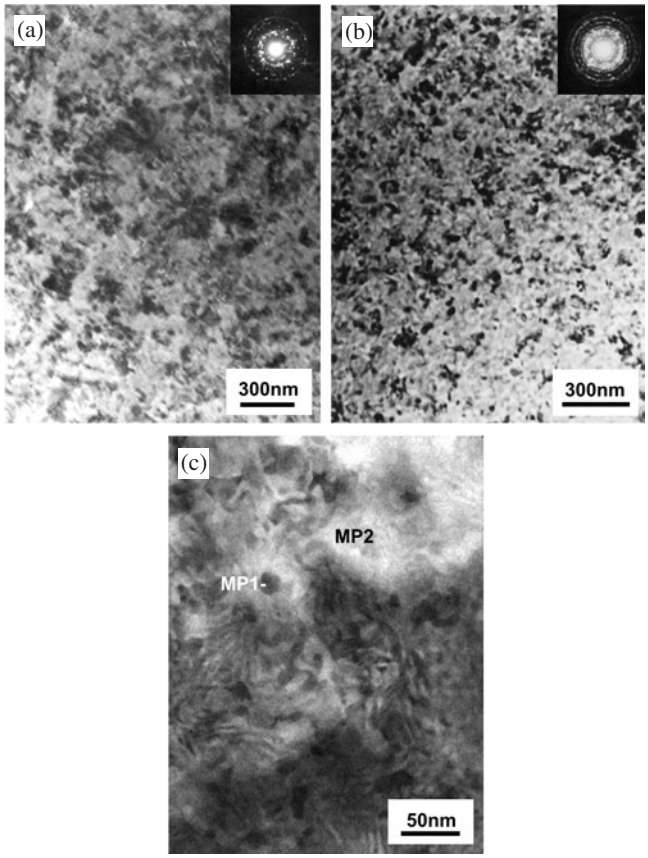

Figure 8. (a) TEM image of $AlLa_{7.7}$ after 185 °C/30 min; diffraction ring patterns in inset. (b) TEM image of $AlLa_{7.7}$ after 230 °C/30 min; diffraction ring patterns in inset. (c) STEM image of $AlLa_{7.7}$ after 230 °C/30 min. Regions MP_i selected for concentration measurements.

measured and analysed in the region between 100 and 320 °C. Additional experiments are done to examine the influence of pre-ageing ('pre') at RT or higher temperatures. The relaxation process can be isolated from the crystallization, if the ER curves derived with respect to time ($d\rho/dt\rho_0$) show a continuous rise followed by a minimum, as in figure 10(a) for $AlLa_{10}$ aged at 130 °C. The first part which can be fitted by a model curve (see section 4.2) having a mean Avrami parameter $\langle n \rangle = 0.5$ reflects the relaxation process and the second part (which passes by a minimum) describes the first crystallization process with $\langle n \rangle \approx 1.5$ leading to the formation of (bcc) structures. The sum of both fits is in fact in good coincidence with the measured curve. The ageing curves are comparable up to 160 °C (figure 10(b)) and the kinetic parameters (see section 4.2) are similar too. At $\vartheta_{ISO} > 160$ °C, the kinetic evolution changes; there is rapid transformation into a further metastable crystalline structure (figure 10(b)) in the case of freshly prepared materials as well as of pre-aged materials. The inset of figure 10(b) shows the ER development (R) as a function of time (t') for the thermal regime with pre-ageing. The first increase of the ER represents the continuous heating (10 K min^{-1}) from RT up to 140 °C; after an intermediate hold at RT (10 min), the transformation at the ageing temperature ϑ_{ISO} occurs within 10 s.

During isothermal ageing at 230 and 250 °C, only the formation of the stable crystalline structures is observable.

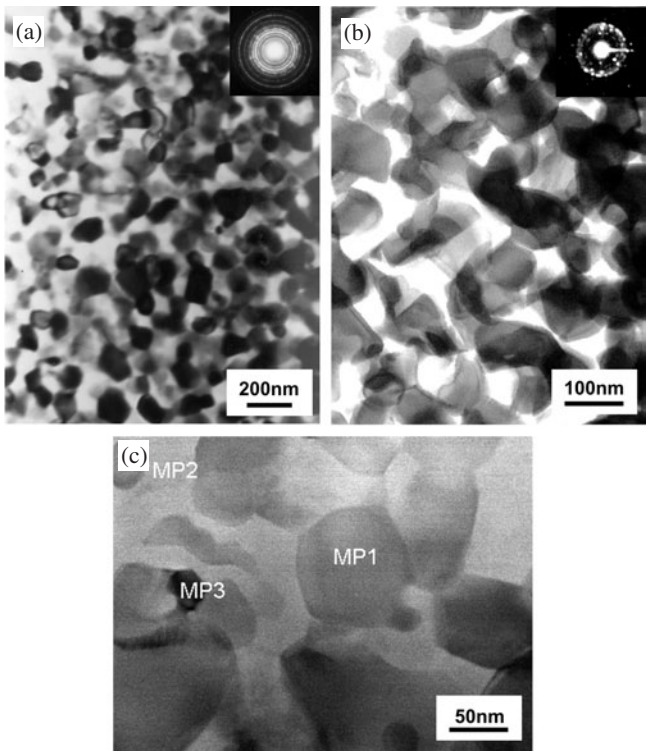

Figure 9. (a) TEM image of $AlLa_{7.7}$ after 260 °C/30 min; diffraction ring patterns in inset. (b) STEM image of $AlLa_{7.7}$ after 260 °C/30 min; diffraction ring patterns in inset. (c) STEM image of $AlLa_{7.7}$ after 250 °C/2 h. Regions MP_i selected for concentration measurements.

3.3.4. Calorimetric studies. Isothermal curves are only exploitable over two restricted temperature intervals. Between 150 and 165 °C (figure 11(a)), the first exothermic effect is ascribed to relaxation. A second effect sets in after a short incubation time and passes by a heat flow minimum. This is typical of a nucleation and growth process; its specific heat is to -24 J g^{-1} and corresponds to the formation of a (metastable bcc) phase. Between 210 and 230 °C (figure 11(b) for 220 °C), two overlapping nucleation and growth processes are observable after the initial decay; they yield about -56 J g^{-1} and accompany the formation of the stable phases, (fcc)Al and (orthorhombic)$Al_{11}La_3$. Activation energies are given in section 4.3.

3.3.5. Microhardness evolution. The results in figure 5 may be interpreted in terms of an irreversible relaxation phenomenon which decreases the hardness in the lower temperature region, followed by short range ordering and transition into the crystalline states which increase the hardness. In isothermally aged amorphous $AlLa_{7.7}$ and $AlLa_{10}$ alloys, initially the hardness shows a similar behaviour (figure 12(a), $\vartheta_{ISO} = 120$ °C). It was proposed that the initial increase results from amplified concentration fluctuations followed by defect annealing and short range ordering. During the structure relaxation the ordering increases and the condition of the cutting of the slip bands improves, hence the hardness decreases. The hardness increases once more during the nucleation and growth of metastable cubic crystals. A partially amorphous material with a very fine dispersion of the crystals (hence a large as-

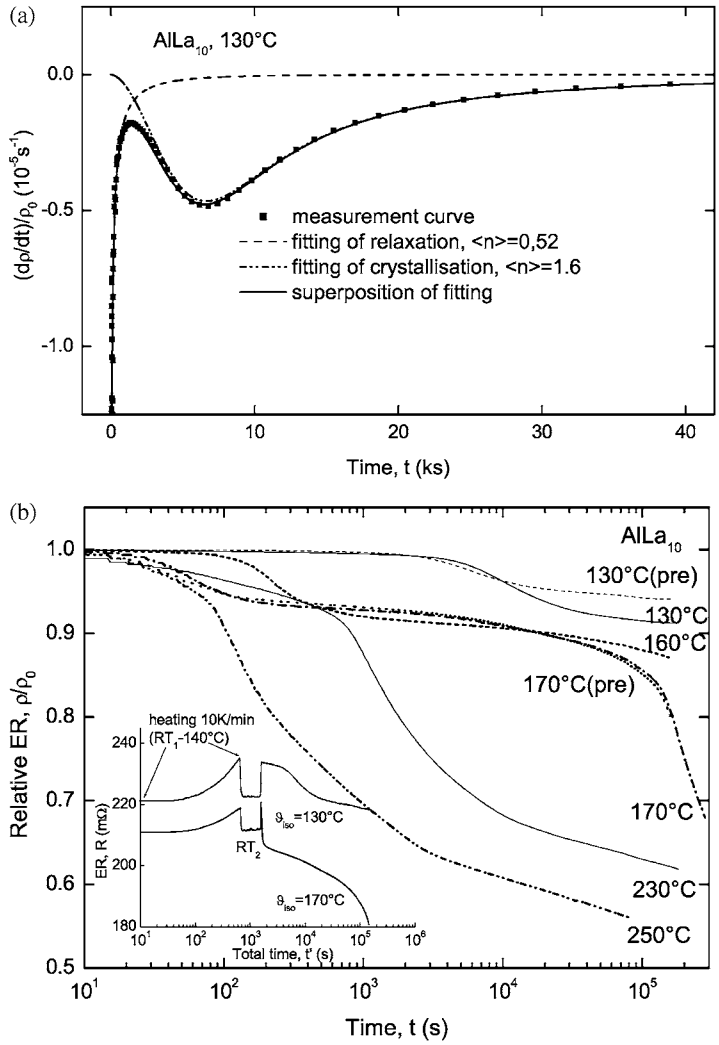

Figure 10. (a) Isothermal ER curve of $AlLa_{10}$ derived with respect to time at 130 °C (full symbols); relaxation (dashed curve, $n = 0.52$) and first crystallization (dash–dot–dot curve, $n = 1.6$) fit curves as well as the sum of both (solid curve). (b) Isothermal ER curves of $AlLa_{10}$ freshly prepared and after pre-ageing (pre); the total thermal regime for the heat treatment with pre-ageing in the inset.

quenched μHV value as in the case of $AlLa_{5.5}$, $\langle d \rangle = 19$ μm) shows only small changes of the μHV during the annealing.

At higher ageing temperatures ($\geqslant$175 °C, see figure 12(b) for $AlLa_{10}$), the spontaneous and the structural relaxations occur so quickly that they cannot be separated from the crystallization. The first maximum corresponds to the formation of bcc structures. The following hardness decrease to a minimum can be interpreted as being due to partial re-dissolution of (bcc) crystals in favour of the precipitation of the stable (fcc)Al and (orthorhombic)$Al_{11}La_3$ phases. The TEM images (figure 8(a)) at 185 °C indeed give the impression that the bcc structure formed at first begins to dissolve. The subsequent hardness increase is caused by the formation of α(fcc)Al and (orthorhombic)$Al_{11}La_3$ in a finely disperse duplex structure (see figure 9(a)).

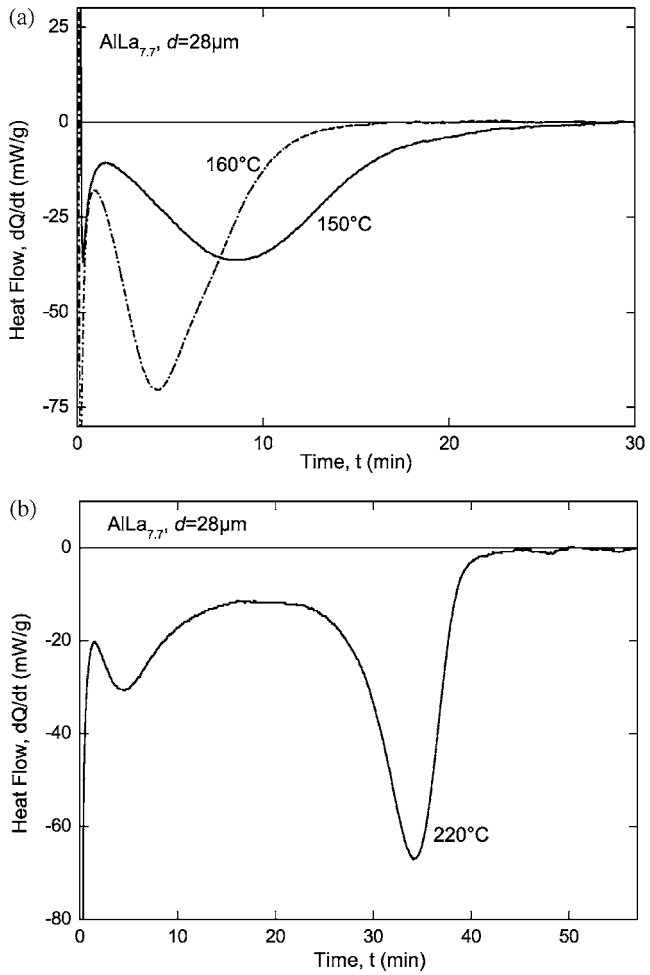

Figure 11. (a) Isothermal calorimetric curves obtained on $AlLa_{7.7}$ at 150 (full curve) and 160 °C (dash–dotted curve). (b) Isothermal calorimetric curves obtained on $AlLa_{7.7}$ at 220 °C.

The dynamics of this process can be estimated from the time shifts between 175 and 250 °C and from the amplitude of the maximum (between 170 and 250 °C). The hardness decrease after the second maximum is due to the grain growth.

4. Determination of structures and kinetic parameters

4.1. The crystalline structure determination

4.1.1. From XRD results. From diffuse amorphous diffraction patterns, the best information is obtained via the determination of the structure factor $S(Q)$ according to Faber and Ziman [18]. Applying this method to the amorphous state in figure 1(e), the following deductions are possible. The main peak corresponds to a shortest atomic distance of 0.25 nm and indicates the dominance of Al–Al bonds. A pre-peak begins to develop during isothermal ageing at $\vartheta \geqslant 150\,^{\circ}\mathrm{C}/30$ min or after long RT ageing. The closest distance in this case is ≈0.48 nm

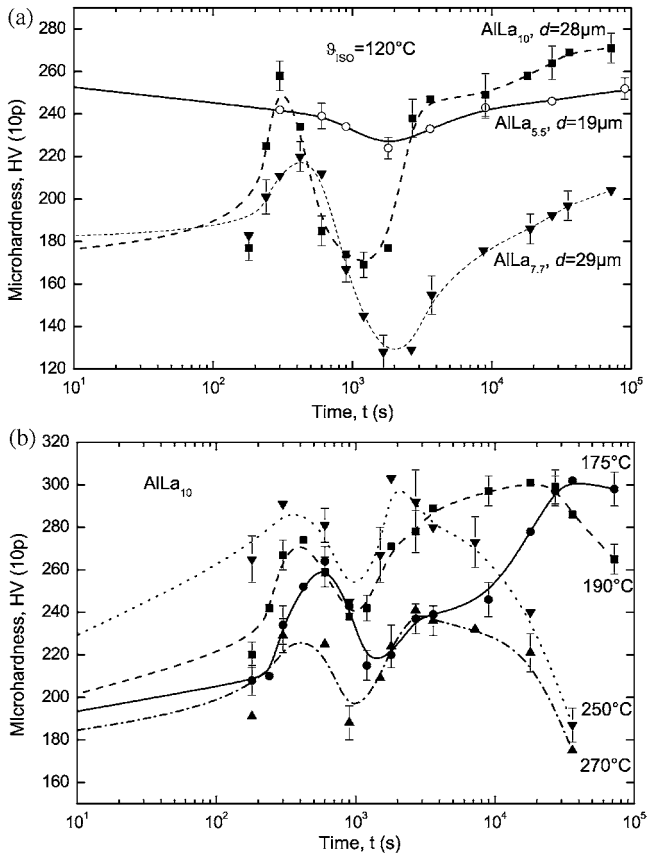

Figure 12. (a) μHV evolution of different AlLa$_x$ ribbons aged at 120 °C (*d*, mean thickness). (b) μHV values of AlLa$_{10}$ after ageing at the temperatures indicated.

and may correspond to Al–La or La–La pairs. According to Monte Carlo simulations on AlLa$_{10}$ [20], Al–La pairs exist in the as-quenched state and are responsible for the pre-peak. This confirms that decomposition begins with clustering.

Crystallization does not start directly with the formation of the equilibrium phases but with a metastable structure, as already shown in section 3.3.1. Different structures are tested using a simulation program, Cerius 2.0. The best agreement with the first crystalline diffraction pattern is found for a bcc structure with $a = 0.33$ nm at temperatures $\vartheta_{ISO} \leqslant 160\,^{\circ}$C, see figure 6(d). At higher temperatures or longer times, the best agreement is achieved for a bcc structure with $a = 0.66$ nm. It corresponds to the single (bcc) phase described by Guo *et al* [6] after annealing at 200 °C. Calculations using Cerius 2.0 give good agreement for the position of the diffraction pattern but not for the intensity. The presence of a bcc structure can be affirmed but the position of the La atoms is not regular over a long distance when the (bcc)AlLa structure develops. No problem exists for the identification of the α(fcc)Al and the (orthorhombic)Al$_{11}$La$_3$ structures during the further transformations.

It will be described in more detail how the kinetics of these transformations can be calculated from the XRD results. First an equipment constant F_{exp} has to be determined because of the different sensitivities of the Al and AlLa phases. The [111] reflex of (fcc)Al and the [132] reflex of the (orthorhombic)Al$_{11}$La$_3$ are compared. The theoretical value of

Table 2. Intensity ratios of the splat cooled samples used for the determination of the correction factors. The error propagation of the intensity ratios is ≈5%.

	$AlLa_{10}$	$AlLa_{7.7}$	$AlLa_{5.5}$	Theoretical value
(fcc)Al I[111]/(fcc)Al I[200]	2.8	2.6	2.1	2.13
(fcc)Al I[111]/(ortho.)$Al_{11}La_3$ I[132]	1.1	1.3	1.7	4.16×10^{-2}
F_{exp}	25.8	31.7	41.1	
F_{cor}	2.6 ± 0.3	2.4 ± 0.3	2.3 ± 0.3	

the intensity ratio is $I[111]/I[123] = 4.16 \times 10^{-2}$. Furthermore, the intensity ratio of the [111] and [200] reflexes of (fcc)Al corresponding to $I[111]/I[200] = 2.13$ will be checked. F_{exp} has to be introduced to account for different La concentrations in the alloys and amounts precipitated as a function of time, the different absorption of the x-rays by the elements, the surface structure of the samples and the decomposition state.

For the determination of F_{exp}, samples produced by splat cooling are used in the as-quenched state. Independent of the La concentration, these crystalline materials have a fine disperse microstructure in the quenched state without perceptible differences in the crystalline structure or the grain sizes. In table 2, the ratios of the experimentally measured intensities for $AlLa_{10}$, $AlLa_{7.7}$ and $AlLa_{5.5}$ and the F_{exp} values are shown. In the last line, the F_{exp}-values are corrected for the concentration by F_{cor}. Knowing the correction factors, the development of the different crystalline structures can be studied. As the diffraction patterns of the different structures overlap, only the change of the intensity will be discussed in the following.

The intensity ratios of (bcc)Al[110]/(bcc)AlLa[211] and (bcc)Al[110]/(bcc)Al[200] of $AlLa_{7.7}$ at 175 °C are shown in figure 13. The ratios were calculated from the values measured during isothermal ageing. The intensity ratio changes with ageing time, if the (bcc)Al structure is the first developed crystalline structure in the amorphous matrix, followed by the (bcc)AlLa structure. The main problem is the validity of the intensity calculation from the atom position in the crystals. If the position of the La atoms is not regular in the unit cell, the intensity of the diffraction reflexes has to be averaged. Nevertheless, a change of the intensity ratio of (bcc)Al[110]/(bcc)AlLa[211] and (bcc)Al[110]/(bcc)Al[200] with ageing time and temperature is found both for $AlLa_{7.7}$ and for $AlLa_{10}$. The increase in the case of the intensity ratio of (bcc)Al[110]/(bcc)AlLa[211] indicates the formation of the (bcc)AlLa structure and the decrease of the intensity ratio of (bcc)Al[110]/(bcc)Al[200] shows the formation of (fcc)Al. After ageing $AlLa_{10}$ for 150 °C/5 min, no diffraction line is found for (bcc)AlLa.

The transformation of the bcc structure into the fcc structure of Al and the orthorhombic structure of $Al_{11}La_3$ can be deduced from the intensity ratio of (fcc)Al[111]/(fcc)Al[200] and the intensity ratio of ((bcc)Al[110] + (fcc)Al[111])/(orthorhombic)$Al_{11}La_3$[123]. Table 3(a) shows that for $AlLa_{7.7}$, the intensity ratio of (fcc)Al approaches the theoretical value with increasing ageing time and temperature. The intensity ratio of Al/$Al_{11}La_3$ decreases. This can be interpreted as being due to increasing amounts of the two phases, (fcc)Al and (orthorhombic)$Al_{11}La_3$.

In table 3b, the results for the formation of the bcc structures after different isothermal ageing treatments of $AlLa_{10}$ are summarized; they show the same tendency as in $AlLa_{7.7}$.

4.1.2. From TEM results. The phase identification from the TEM images and the diffraction patterns must agree with the XRD results. The exploitation of TEM diffraction patterns is, however, much more complicated than of XRD patterns. The lattice constant, a, has to be determined from the experimentally determined $d_{(hkl)}$-spacing and the (hkl)-values of each

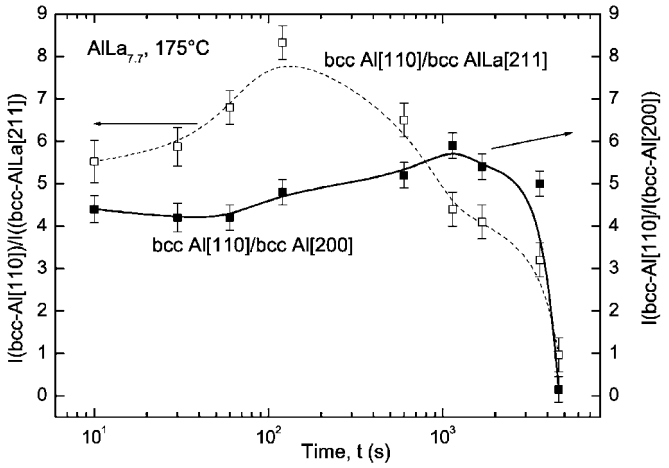

Figure 13. Variation of XRD intensity ratios of $AlLa_{7.7}$ at 175 °C (bcc structures).

Table 3. (a) Intensity ratios of (fcc)Al[111]/(fcc)Al[200] and ((bcc)Al[110] + (fcc)Al[111])/(ortho.)$Al_{11}La_3$[123] of $AlLa_{7.7}$ at different temperatures and ageing times. (b) Intensity ratios of (bcc)Al[110]/(bcc)AlLa[211] and (bcc)Al[110]/(bcc)Al[200] of $AlLa_{10}$ at 150 and 175 °C after different ageing times. The error propagation of the intensity ratios is ≈5%.

ϑ (°C)/t (min)	I(fcc)Al[111]/I(fcc)Al[200]		I((bcc)Al[110] + (fcc)Al[111]/ I(ortho.)$Al_{11}La_3$[123]
175/4620	2.6	(bcc)Al transforms to (fcc)Al	0.92
230/10	5.5	(fcc)Al increases, (bcc)AlLa exists	2.13 (ortho.)$Al_{11}La_3$ part small
230/30	6.6		0.96
250/10	3.5	(bcc)AlLa vanish	0.94
250/30	2.1		0.74
250/840	1.7	Theoretical value: 2.12	0.85 Exp. splat cooling: 1.23
ϑ (°C)/t (min)	I(bcc)Al[110]/I(bcc)AlLa[211]	I(bcc)Al[110]/I(bcc)Al[200]	
150/5	(bcc)AlLa does not exist	4.8 (bcc)Al	
150/30	5.6	5.6	
150/3400	5.5	4.6	
175/10	8	6.8	
175/30	6	6.2	

diffracting plane according to $a = (h^2 + k^2 + l^2)^{1/2} \cdot d_{(hkl)}$. The $d_{(hkl)}$-spacing is determined with the device constants $d_{(hkl)} = \lambda * L * f/R$ (with $\lambda * L = 1.7297\ \mu m^2$, $f = 1.6$); R is half of the diameter of the diffraction ring or the distance between the diffraction spots. Applying the selection rules for different crystalline structures, a correlation between the measured diffraction peaks and the calculated diffraction spots is possible [22].

The intensity (I) is proportional to the square of the structure factor ($|F_{hkl}|^2$) [23]. This method is taken into account too for the XRD calculation with the program Cerius 2.0. Because the atomic form factor of the La atoms is greater than for the Al atoms, it is more dominant.

For the as-quenched state of $AlLa_{7.7}$, the TEM (figure 2(c)) and STEM diffraction images show a diffuse ring pattern with a d-spacing value of (0.25 ± 0.04) nm. This value is in

good coincidence with the calculated minimum of the atomic distance (0.245 nm) from the structure factors. After ageing for 30 min at 175 °C, the analysis of several diffraction ring patterns in figure 7(a) and the spot patterns in figure 7(b) of the TEM image allowed us to correlate the reflexes of the (bcc)Al ([110], [200] and [220]) and (bcc)AlLa ([110], [200], [211], [310], [411 + 330] and [422]). The [220] and [422] reflexes are overlapped. The ring pattern of the STEM image in figure 7(c) could be assigned to the (bcc)Al [110] reflex. The corresponding lattice parameters were determined to be $a = (0.33 \pm 0.01)$ nm for (bcc)Al and $a = 0.66 \pm 0.01)$ nm for (bcc)AlLa.

The $d_{(hkl)}$-values determined from the ring patterns of the diffraction images in figures 9(a) (TEM) and (b) (STEM) are in good agreement with the most intensive reflexes of the stable (orthorhombic)$Al_{11}La_3$ ($a = 0.4431$ nm, $b = 1.0132$ nm, $c = 1.3142$ nm) and of the (fcc)Al ($a = 0.4049$ nm) phases. The data calculated with the help of the software Cerius 2.0 and the results of the literature [15] agree well.

The element intensity distribution confirmed the phase identification. The concentration ratios of Al and La were determined again from the relation $c_{La}/c_{Al} = k_{AlLa} \cdot I_{La}/I_{Al}$. Experimental results relative to the mean concentrations across the samples as well as to selected sample regions (MP_i) are given for the as-quenched state in section 3.1 and for aged states (230 °C/30 min and 260 °C/30 min) in section 3.3.2.

After ageing at 175 °C/10 min, the measurement of the intensity distribution was not successful because of the small size of the particles. If we interpret the small particles in figure 7(c) as crystals at the beginning of the crystallization, their density can be estimated. 12 crystals are found in an area of 0.381 μm^2; their mean size is 50 nm. If the crystals grow isotropically in all directions, the final state has an area of 30 000 nm^2 or a mean length of 122 nm. The largest particles which are found at 175 °C/120 h have a dimension of 412 nm. This means that the bcc particles combine during the ageing process.

4.2. Determination of the kinetic parameter

The evolution of the kinetic or Avrami parameter n is important for the understanding of the transformation processes in amorphous materials. The investigation of other amorphous Al-rich materials has shown that they are controlled by nucleation and growth but cannot be described by the simple form of the JMAK model [9]. Therefore other models are chosen, namely a more general JMAK model (GM) [9] and a description with the local kinetic parameter n_{loc} [10].

First, the fraction transformed, $\alpha(t)$, is calculated from the isothermal ER curves:

$$\alpha(t) = \frac{\rho_0 - \rho(t)}{\rho_0 - \rho_c}$$

The modelling of this fraction within the frame of the GM is done by applying the following equation:

$$\alpha(t) = 1 - \left[\frac{\left(\frac{t}{\tau_\eta}\right)^{n_\eta}}{\eta} + 1 \right]^{-\eta}$$

with η being the impingement parameter, n_η the kinetic parameter and τ_η the characteristic transition time [9].

GM modelling is applied to ER measurements of the first transformation in $AlLa_{7.7}$ (figure 14(a)) and $AlLa_{10}$ (figure 14(b)). As already shown for a derived curve in figure 10(a), the initial part due to relaxation can be isolated and fitted with the JMAK model giving $\langle n \rangle$-values of about 0.5. These values were found for relaxation in other amorphous materials

Table 4. General model (GM) results for isothermal aged $AlLa_{10}$ without and with pre-ageing. Without: isothermal ageing at ϑ_{ISO}. With: with pre ageing in the regime RT to 140 °C (5 K min^{-1}), RT (15 min), ϑ_{ISO}. η, impingement parameter; $\langle n_\eta \rangle$, kinetic exponent of the GM; $t_{\alpha=0.63}$, time at $\alpha = 0.63$; $n_{\alpha=0.63}$, kinetic exponent at $\alpha = 0.63$; $\Delta\rho/\rho_{ISO,10s} = (\rho_{ISO,10s} - \rho_{cry})/\rho_{ISO,10s}$. Standard deviation of the fit values: <1%.

	$t_{\alpha=0.63}$ (s)		η		n_η		$n_{\alpha=0.63}$		$\Delta\rho/\rho_{ISO,10s}$ (%)	
ϑ_{ISO} (°C)	Without	With	Without	With	Without	With	Without	With	Without	With
130	17 500	9300	0.44	0.50	2.58	2.45	1.63	1.48	8.31	5.23
140	4 150	3870	0.47	0.79	2.60	2.09	1.55	1.43	8.67	6.07
150	1 340	520	0.56	0.76	2.05	2.86	1.28	1.94	8.23	8.15
160	235	305	1.11	0.41	3.30	3.70	2.45	2.12	7.75	8.11
170	80	64	0.61	0.92	2.65	2.14	1.69	1.51	6.87	6.49

too [11, 12]. ρ/ρ_0-results for $AlLa_{7.7}$ (full curves in figure 14(a)) together with the model curves for the first crystallization process (symbols) show that the various crystallization products add differently to the ER. The relaxation part contributes to ER changes by about 2%; the formation of (bcc)Al by about 10%, (bcc)Al and (bcc)AlLa by about 23% and (bcc)AlLa alone by about 12%.

Compared to $AlLa_{7.7}$, $AlLa_{10}$ (figure 14(b)) possesses faster kinetics perhaps due to stronger relaxation during RT storage. But the results are not essentially different. The fitting parameters, τ_η, η, n_η, $\rho(\alpha = 0)$ and $\rho(\alpha = 1)$ are determined with the GM. In table 4, the parameters η and n_η are shown together with the parameters $t_{\alpha=0.63}$, $n_{\alpha=0.63}$ and $\Delta\rho/\rho_{10s}$ ($\Delta\rho = \rho(\alpha = 0) - \rho(\alpha = 1)$) deduced from the GM for $AlLa_{10}$ as described in [9]. It is interesting to note that the values of the kinetic parameters n_η and $n_{\alpha=0.63}$ change at 160 °C. At lower ageing temperatures, the values for $n_{\alpha=0.63}$ are <2. At 160 °C, the $n_{\alpha=0.63}$ value increases to 2.5. Above 170 °C, the kinetic parameters decrease again. In agreement with the XRD results and TEM images, the formation of the (bcc)Al crystals takes place at <160 °C, but at 160 °C (bcc)AlLa is formed additionally. The higher n value can be interpreted in favour of the necessity of nucleation at constant rate [8]. In order to test this idea, different experiments with pre-ageing were performed (see results on $AlLa_{10}$ in figure 14(c)). They will be discussed in section 5.

In figure 15, the $n_{loc}(\alpha)$ results for $AlLa_{10}$, calculated as described in [10], confirm that the behaviour changes at about 160 °C. The agreement between $n_{loc}(\alpha)$ and $n(\alpha)$ from the GM is quite satisfactory.

The modelling of the isothermal ER curves at higher temperatures proves to be difficult because of the complex character of the second crystallization reaction leading to the stable phases (fcc)Al and $Al_{11}La_3$. The values calculated for the fraction transformed, α_2, are given in figure 16(a). The second crystallization is isolated (see inset of figure 16(a)) according to $\alpha_2(t) = (\rho_{02} - \rho_2(t))/(\rho_{02} - \rho_{E2})$ with new start values ρ_{02} and final values ρ_{E2}. The determination of the n_{loc}-values confirms the presence of two processes, formation of (fcc)Al and (orthorhombic)AlLa. At the beginning, the $n_{loc(\alpha 2)}$-values are of the order of 2.5, but decrease to about unity before they increase at $\alpha \approx 0.4$ and then drop to 0.5 (figure 16(b)). Looking for a possible interpretation, it can be admitted that the second crystallization process begins with the formation of nuclei at a constant rate. Together with the μHV results and the TEM images at 185 °C, this agrees with the previous dissolution of the first (bcc)crystalline structures (probably only (bcc)AlLa). Results of the GM fits support these conclusions.

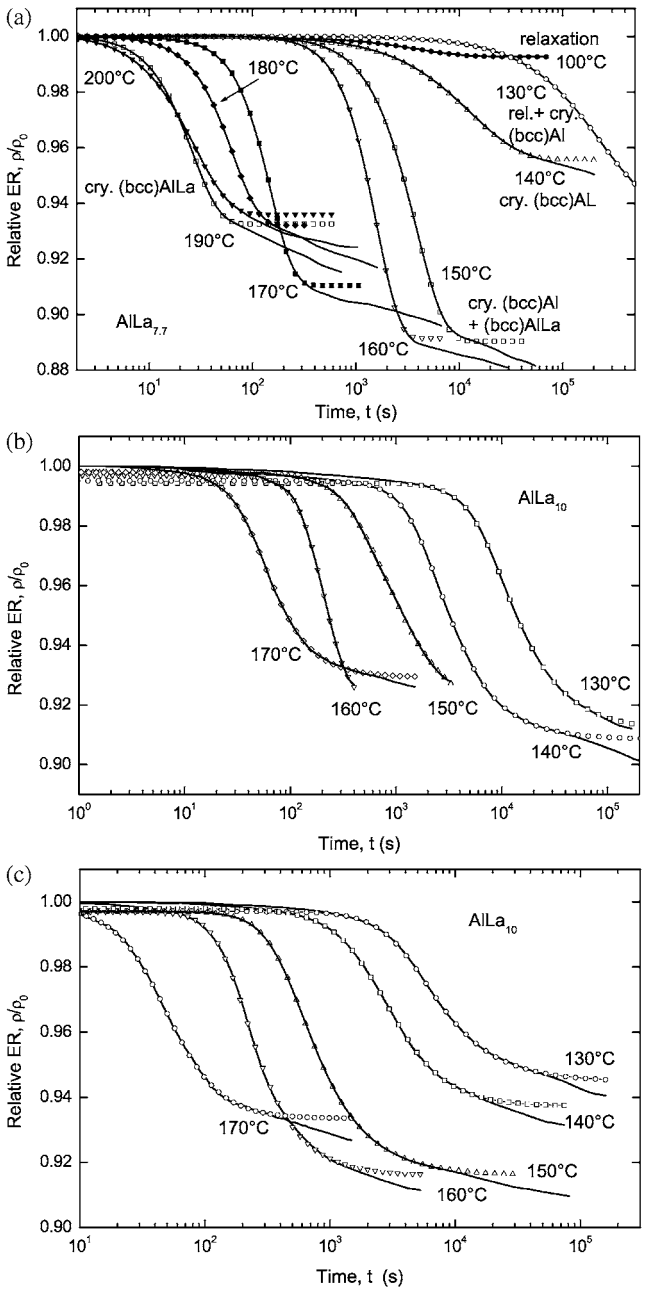

Figure 14. (a) Isothermal ER curves (curves) together with the model fitting curves (symbols) for $AlLa_{7.7}$ in the temperature interval 100–200 °C. (b) Isothermal ER curves (curves) together with the model fitting curves (full symbols) for $AlLa_{10}$ in the temperature interval 130–170 °C. (c) Isothermal ER curves (curves) together with the model fitting curves (open symbols) for $AlLa_{10}$ in the temperature interval 130–170 °C after pre-ageing (heating to 140 °C at 5 K min^{-1}, RT and ϑ_{ISO}).

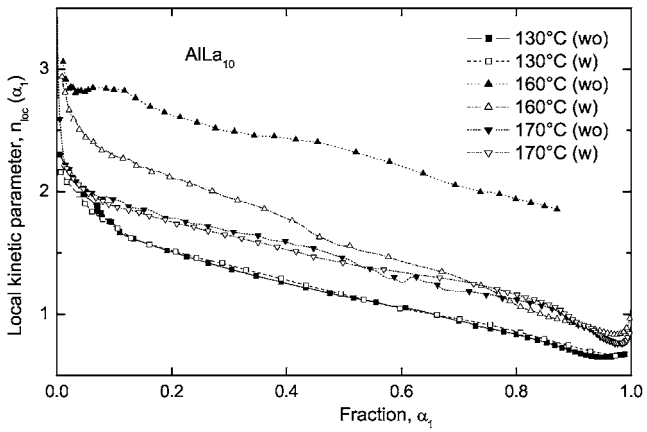

Figure 15. Evolution of $n_{loc}(\alpha)$ in the temperature range 130–170 °C with (open symbols) and without pre-ageing (full symbols) of $AlLa_{10}$, for crystallization only.

4.3. Determination of the activation energy

Assuming the validity of the Arrhenius equation, the activation energy of the amorphous to crystalline transformation can be derived from GM modelling at $\alpha = 0.63$. This value is equivalent to the one derived from the JMAK model [11, 14] in the case of isothermal ageing (E_{iso}) or from the Kissinger plot (E_Q) in the case of DSC experiments [13]. It comprises the energies necessary to form nuclei of overcritical size and/or to assure their growth by diffusion. Starting from this concept, an activation energy which varies during the transformation process is possible.

Applying the Kissinger analysis to DSC curves of $AlLa_{7.7}$ obtained at four different heating rates, the mean E_Q-values for the first, second and third peak are (1.68 ± 0.10), (2.0 ± 0.2) and (1.93 ± 0.10) eV, respectively. The same analysis for $AlLa_{10}$ results in (1.73 ± 0.10) eV for the first, (1.81 ± 0.20) and (1.87 ± 0.10) eV for the second and third peaks.

The pre-exponential factor k_0 in the Arrhenius equation $k_T = k_0 \exp(-E_{iso}/(k_B T))$ represents the transformation rate at a given temperature. The $\langle \ln(k_0) \rangle$ value derived from the Arrhenius plot is (50.6 ± 0.4) for the first crystallization of $AlLa_{10}$ when linearization over the entire isothermal region. It corresponds to 9.6×10^{21} s^{-1}. A fit of the first transformation in $AlLa_{7.7}$ leads to $\ln(k_0) = (43.2 \pm 4.3)$, hence 5.9×10^{18} s^{-1}.

The value of the mean activation energy is very sensitive to the temperature interval of isothermal ageing yet calorimetric curves are exploitable only in restricted intervals. Between 150 and 165 °C, the time shift of the first minimum yields an E_{iso}-value of (1.6 ± 0.2) eV of $AlLa_{7.7}$ and (1.8 ± 0.1) eV of $AlLa_{10}$. Between 210 and 230 °C, two overlapping nucleation and growth processes are observed and have mean E_{iso}-values of (1.8 ± 0.10) and (2.2 ± 0.2) eV in the case of $AlLa_{7.7}$.

The analysis of the isothermal ER results in a much wider temperature interval (120–190 °C) results in $E_{iso} = (1.89 \pm 0.10)$ eV for the first crystallization process in $AlLa_{7.7}$ (figure 17(a), full symbols). A change of the $\ln \tau$ $(= \ln(1/k_T))$ values is observable at 160 °C for $AlLa_{7.7}$. Taking this fact into account and performing fits in two intervals, 120–150 °C and 160–190 °C, two different E_{iso}-values are obtained, (1.50 ± 0.05) and (1.33 ± 0.06) eV, respectively. In the case of $AlLa_{10}$ (figure 17(b), full symbols), such a change occurs at 150 °C. The mean activation energy in the interval 130–170 °C is (2.1 ± 0.1) eV. The reason for this unusual result is the complex crystallization process which cannot be described adequately by

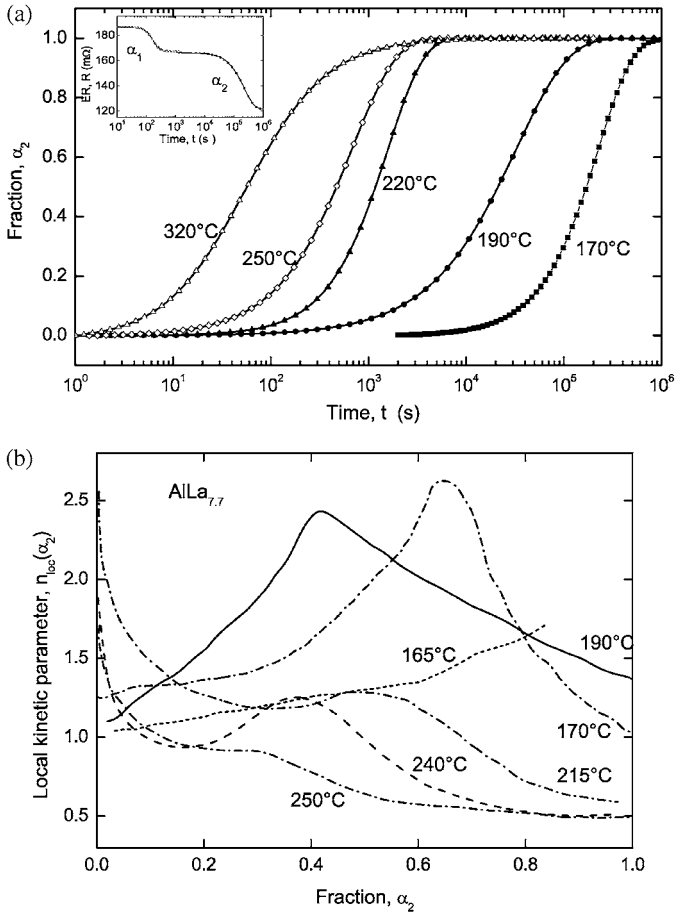

Figure 16. (a) Behaviour of α_2 during the second crystallization of $AlLa_{7.7}$ between 170 and 320 °C leading to (fcc)Al and (orthorhombic)$Al_{11}La_3$. In the inset, the complete ER curve for 170 °C; the intersection of the horizontal line with the experimental curve shows the beginning of the second crystallization. (b) Variation of $n_{loc}(\alpha_2)$ for $AlLa_{7.7}$ in the temperature region 165–250 °C.

mean values. Therefore the activation energy was recalculated as a function of the crystalline fraction $\alpha(t)$ (in steps of 0.1 between $\alpha = 0.1$ and 0.9) for different temperatures T_{iso}, using the concept of local kinetic parameters, $n_{loc}(\alpha(t))$, in the following representation:

$$E_{ISO}(\alpha) = k_B T_{ISO}\left[\ln(t(\alpha)k_0) - \frac{\ln(-\ln(1-\alpha(t)))}{n_{loc}(\alpha(t))}\right].$$

If the $n_{loc}(\alpha(t))$-values are nearly constant during the transformation, the activation energy for each T_{iso} is constant too. When $n_{loc}(\alpha(t))$ varies, the calculation is more extensive. Examples are given in figure 18(a); they apply to $AlLa_{7.7}$ aged in the temperature interval 100–170 °C. In the region of relaxation at 100 °C, the activation energy is almost constant between $\alpha = 0.1$ and 0.9, if relaxation is assimilated to a precipitation process. Between 120 and 145 °C, the activation energy starts with small values (nucleation) and increases continuously up to 1.8 eV. Between 150 and 180 °C, the activation energy is higher and decreases with the onset of the formation of bcc AlLa crystals. This behaviour is observed only for the crystallization processes leading to the formation of (bcc)Al or (bcc)AlLa. For $AlLa_{10}$, the same calculations

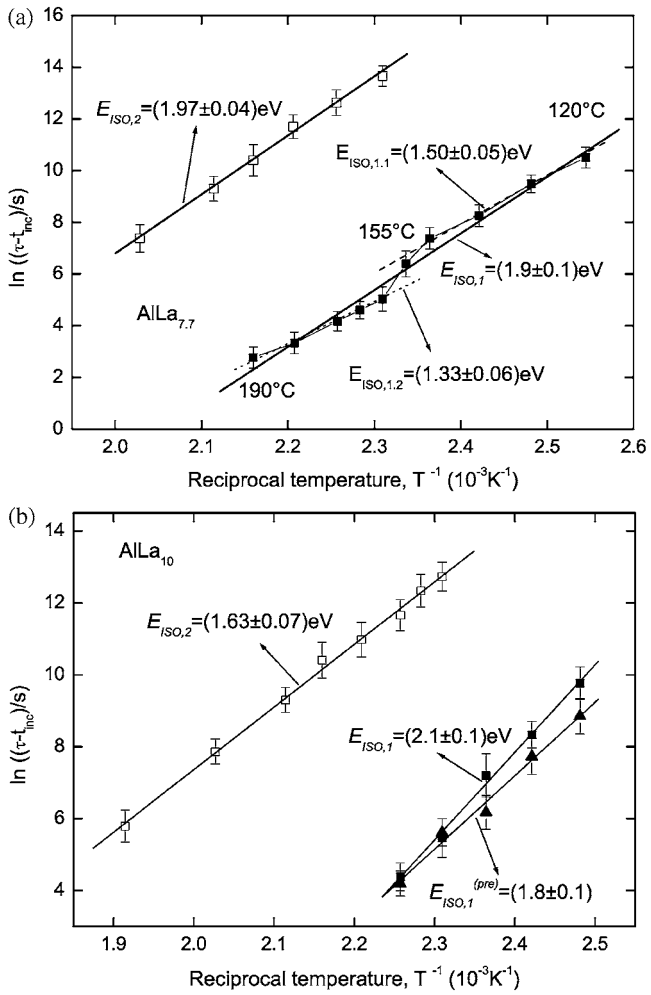

Figure 17. (a) Arrhenius plot for isothermal ageing of $AlLa_{7.7}$ between 120 and 190 °C (first crystallization, full square) and between 160 and 220 °C (second crystallization, open square) applying GM results. (b) Arrhenius plot for isothermal ageing of $AlLa_{10}$ between 130 and 170 °C (first crystallization), with (full triangle) and without (full square) pre-ageing and between 160 and 250 °C (second crystallization, open square) applying GM results.

give the results reproduced in figure 18(b). Between 130 and 150 °C the $E_{ISO}(\alpha)$ increases. The nucleation and forming of the (bcc) structures lead to the higher $E_{ISO}(\alpha)$-values.

From the second slope of the isothermal ER curves (formation of the stable phases (fcc)Al and (orthorhombic)$Al_{11}La_3$, mean activation energies are fitted in the temperature interval of 160–250 °C with the help of the Arrhenius plot (included in figures 17(a), (b), open symbols). For $AlLa_{7.7}$ $E_{iso,2} = (1.97 \pm 0.04)$ eV and for $AlLa_{10}$ $E_{iso,2} = (1.63 \pm 0.07)$ eV.

5. Influence of pre-ageing on the transformation process

Natural ageing over several years (>3 years) does not change the decomposition behaviour but the transformation kinetics becomes faster. Such acceleration is found after artificial ageing

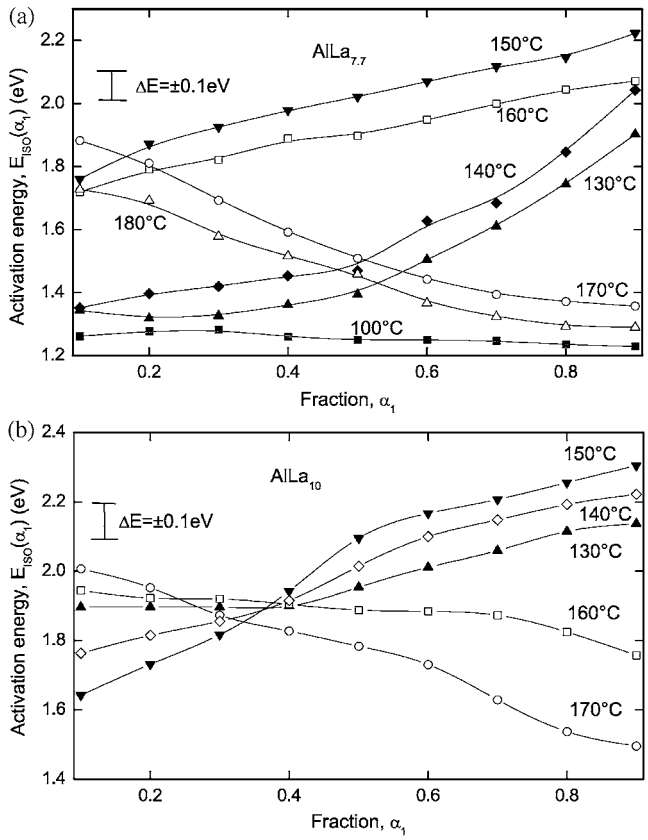

Figure 18. (a) $E_{iso}(\alpha_1)$-variation of $AlLa_{7.7}$ with varying $n(\alpha_1)$-values in the temperature range 100–170 °C. (b) $E_{iso}(\alpha_1)$-variation of $AlLa_{10}$ with varying $n(\alpha_1)$-values in the temperature range 130–170 °C.

too. In consequence, crystallization is observed at lower temperatures in the observed time interval $t < 10^5$ s.

The influence of pre-ageing is investigated systematically after heating the materials from RT to 140 °C at 10 K min^{-1}, quenching to RT and isothermal ageing at ϑ_{iso} between 130 and 170 °C (see inset of figure 10(b)). The first transformation together with its modelling (GM) is shown in figure 14(c). At 130 and 140 °C, nucleation and growth during the crystallization process is accelerated as relaxation has taken place partly during heating. At $\vartheta > 140$ °C, a still remaining relaxation is very difficult to detect. But the influence of pre-ageing can be evaluated from the relative change of the specific ER without and with pre-ageing and the τ-values. A comparison of the kinetic values shows a decrease of the $\langle n \rangle$-values after pre-ageing, with a change in the region of 160 °C. At the beginning, the $n_{loc}(\alpha)$-value is high but quickly decreases to unity at $\alpha = 0.63$. Although pre-ageing up to 140 °C influences the relaxation, a nucleation process takes place during the isothermal ageing before the crystallization. The shift of the n_η- and $n_{\alpha=0.63}$-values with ϑ_{ISO} is in agreement with the acceleration (table 4).

The mean activation energy for the first crystallization to (bcc) structures is determined from the Arrhenius plot after performing GM modelling and turns out to be (1.8 ± 0.1) eV.

6. Discussion

The phase diagram of the Al–La system [21] indicates that in the liquid state there is complete miscibility between the Al and La atoms, whereas in the solid state solubilities are extremely small. During solidification, demixing has to occur provided that diffusion is high enough to reorganize the liquid structure into an fcc and an orthorhombic structure. If rapid cooling by melt-spinning retains a liquid-like structure with strong concentration fluctuations announcing phase separation, it is conceivable that bcc structures with the big La atoms in the central positions form first upon annealing. At still higher temperatures, La diffuses out of these bcc phases and participates in the formation of $Al_{11}La_3$. Hence decomposition starts with (kinetically favoured) bcc phases which are finally replaced by the (energetically favoured) equilibrium phases.

The structure of the amorphous state is described as a closest packed structure [24]. Investigations on an amorphous AlY_{10} alloy [25] with anomalous XRD resulted in atomic distances of <0.3 nm for Al–Al, ≈ 0.32 nm for Al–Y and ≈ 0.36 nm for Y–Y. The co-ordination numbers allow the conclusion that one central Y atom is surrounded by four Al atoms; Y–Y pairs were not found. This result confirms the compound formation tendency in Al–Ln materials [2]. The authors in [21, 26] attribute this effect to the rare-earth atomic collapse in the formation of Al-rich metallic glasses.

Partial shortening of the Al–La bonds decreases the size mismatch between the Al and La atoms and explains the glass forming ability of $AlLa_9$ [17].

According to SAXS investigations [7], different regions coexist in the amorphous as-quenched structure. The calculated correlation function and the determination of the mean distribution give the same conclusions, i.e. a size distribution exists with a mean value of 150 nm. There are two possible interpretations:

- differences in the density between the two regions exist or
- differences in the concentration of the elements lead to La-rich and La-poor regions.

In the case of differences in the density, the scattering curves of the as-quenched state (amorphous) and after ageing at 175 °C/30 min (crystalline) should be distinguishable. As such a behaviour is not observed, we attribute the different scattering regions to concentration variations. Since the element distribution between the as-quenched state and the state obtained after 175 °C/30 min has not changed either, this interpretation is suited. The concentration fluctuations in the Al–La materials already exist in the melt or form during the quenching and may even get amplified. Upon rapid solidification, regions with higher and with lower La concentrations are formed in the ribbons starting from these concentration fluctuations; they are frozen in and form two penetrating amorphous structures without sharp interfaces.

With the help of the pair correlation function which is proportional to the structure function $S(Q)$, we can obtain information about the mean distance of several coordination shells for any atom. The wavevector Q at the first maximum of $S(Q)$ is inversely proportional to the average distance between the nearest neighbours: $q \approx 2\pi/r$. Assuming only one scattering curve, we obtain $q = 4\pi(38°/2)/0.154 = 0.2338$ nm^{-1} and $r \approx 2\pi/q = 0.27$ nm for the binary Al–La materials. Only small shifts are needed for the transformation of the amorphous structure into the bcc lattice structure.

The TEM images confirm the results from the XRD, calorimetry and ER measurements. They also show that the initially formed crystalline regions have very different sizes and are rather unstable. From time to time the electron beam heating was sufficient to transform the bcc structure. For all the materials investigated by TEM, the ribbons had a fine disperse structure, and in the final state the size distribution of the stable phases was identical with the grain structure.

The evolution of the kinetic parameter $n(\alpha)$ determined by the GM and the local modelling confirms the existence of an early nucleation process coupled with growth. Only when the formation of (bcc)Al crystals is well in progress do (bcc)AlLa crystals begin to form due to the slower diffusion of the big La atoms. The increase of the activation energy can be taken as a confirmation for this fact.

The μHV curves and TEM images indicate that the transition to the stable phases is linked to a partial dissolution of the bcc structure. The transition of(bcc)Al crystals into (fcc)Al is expected to present no problems, but the (orthorhombic)$Al_{11}La_3$ structure needs La atoms and a reorientation of the (bcc)AlLa structure. The structure changes can occur in two extreme ways.

- A direct transformation of the bcc structures into the (fcc)Al and (orthorhombic)$Al_{11}La_3$ phases.
- Dissolution of the bcc structures and formation of a kind of solid solution which decomposes at higher temperature and forms the stable phases.

We propose that the (bcc)Al regions transform directly to (fcc)Al by emitting La atoms into the matrix, whereas the majority of (bcc)AlLa dissolves and orthorhombic $Al_{11}La_3$ forms according to a nucleation and growth mechanism by uptake of La. The kinetic parameters calculated via the GM and in the form of n_{loc} support nucleation of crystals at a constant rate (see below).

The amorphous Al–La alloys are very good examples for the determination of local activation energies which can be interpreted in the light of different structures formed. In most publications, only mean activation energies are cited. The formation of (bcc)Al requires an almost constant energy because nuclei exist in the amorphous state or will be formed during the relaxation. The fitted value $n_{\alpha=0.63} \approx 1.5$ describes the growth of small particles by diffusion. The crystallization of the La-rich regions ((bcc)AlLa) is more complex. At the beginning, the activation energy is high and nucleation and growth probably co-operate; the n-value of 2.5 confirms this process. When growth becomes dominant, the activation energy is similar to that for (bcc)Al. The activation energy estimates from ER experiments are very sensitive to the first transformation (amorphous to bcc crystalline). The calorimetric measurements are more sensitive to the following crystalline transformations leading to two phases of different thermal stabilities and having different activation energies of formation (1.8 and 2.2 eV).

The correct interpretation of the crystallization of the amorphous state also requires an understanding of the relaxation processes which the materials undergo. Relaxation can be studied in different kinds of experiment. In XRD, the development of a pre-peak is an essential indication of structural relaxation. In isothermal calorimetric and ER measurements, relaxation is accompanied by a slow decrease of the exothermal heat flow and of the ER. If crystallization sets in late, both effects, relaxation and crystallization, can be fitted separately. The best adjustment of the JMAK-fit curves to the relaxation part is given for $n \approx 0.5$. In former investigations on AlDyNi [12], it was shown that such a result is an approximation to the $\ln t$ plot which Gibbs *et al* [27] developed for the relaxation. In the Al–La materials, the modelling of the relaxation by the $\ln t$ plot is less good.

The intensive study of activation energies via different experimental approaches (isothermal and non-isothermal ER as well as calorimetric measurements) yields about the same mean values. The reason for discrepancies in isothermal measurements can be traced back to the temperature interval covered and to the manner in which thermal equilibrium is achieved. In calorimetric experiments, the isothermal ageing temperature is obtained after heating from RT to ϑ at about 200 K min^{-1}; only a small temperature interval can be investigated. In ER measurements, less than 10 s is necessary.

In the latter type of experiment, firstly an activation energy $E_{ISO}(\alpha)$ is estimated for different temperatures. The fits with the help of the Avrami equation show deviations and yield only approximate values. Whereas the activation energy for the relaxation process is nearly constant ($\approx$1.25 eV), the formation of the (bcc)Al crystals needs a higher activation energy (up to $\approx$1.8 eV). The energy increases once more during the formation of the (bcc)AlLa crystals (to 2.2 eV) then falls below 1.4 eV at the end. Different mean activation energy values derived from the Avrami plot of experimental results obtained by different methods (e.g. calorimetry and ER) reflect different sensitivities to the crystal formation processes. The ER is more sensitive to small changes of the inner atomic structure than thermal properties. As only small sample masses could be employed, DSC did not even show up the existence of two bcc structures.

7. Conclusions

Amorphization of Al-rich La alloys is possible in a limited concentration range despite a prohibitive size mismatch counterbalanced by the lanthanide contraction. At small La concentrations, the equilibrium phases, α(fcc)Al and $Al_{11}La_3$, precipitate after melt-spinning. High wheel speeds promote the formation of amorphous states on the substrate side of $AlLa_{5.5}$. Fully amorphous structures are retained in the case of $AlLa_{7.7}$ and $AlLa_{10}$ up to a ribbon thickness of about 30 μm.

In dependence on the cooling rate, the equilibrium phases or the metastable (bcc)Al phase are formed in $AlLa_{7.7}$ or the alloy is retained in an amorphous state. This different behaviour can be traced back to kinetic problems. If the Al atoms do not have sufficient time for migration during cooling, the quenched-in liquid state shows strong concentration fluctuations preceding phase separation, but still remains amorphous. If the Al atoms can diffuse sufficiently during cooling, they are able to take up ordered positions and form a bcc structure in the as-quenched state. It is embedded between amorphous regions of higher La concentrations where diffusion is more difficult due to the bigger size of the La atoms. Given enough time, complete decomposition into the stable (fcc)Al and $Al_{11}La_3$ phases can be achieved during cooling.

Relaxation phenomena can be observed in amorphous alloys. An irreversible evolution occurs during RT storage and ageing at more elevated temperatures as further demixing and annealing of quenched-in defects take place. The presence of a reversible relaxation process due to short range order changes is ascertained from the existence of pre-peaks in XRD patterns and microhardness (μHV) increases.

ER, XRD and TEM studies show that the first crystallization reaction leads to the development of metastable bcc structures, first (bcc)Al having a lattice parameter of 0.33 nm, followed by (bcc)AlLa with a parameter of 0.66 nm. Both phases are present in $AlLa_{10}$ after 30 min annealing at 150 °C. Calorimetry confirms that the process is controlled by nucleation and growth, but cannot distinguish between the two bcc phases which possess higher μHV values than the amorphous state. During long time ageing at temperatures $>$ 160 °C, the metastable phases are replaced by the stable precipitates, α(fcc)Al and orthorhombic $Al_{11}La_3$. Evidence for partial re-dissolution (probably only concerning (bcc)AlLa) before the precipitation of the equilibrium phases comes from TEM and μHV results which also indicate the correlation between high hardness values and the presence of a fine duplex structure. At temperatures $\geqslant$200 °C, separate nucleation and growth processes for the stable phases can be discerned in calorimetric studies.

Mean and local kinetic parameters (Avrami exponent and activation energy) were derived from isothermal ER measurements with the help of a general JMAK model. They confirm

that the crystallization behaviour changes around 160 °C and that precipitation at higher temperatures involves fresh nucleation. Mean activation energies deduced from ER and calorimetric experiments at constant temperatures and at different heating rates agree fairly well. The low values obtained ($\leqslant$2 eV) reflect the great instability of amorphous Al–La alloys in comparison to Al–La–T and Al–Ln(–T) alloys. The irreversible relaxation process does not stabilize the amorphous state. Pre-ageing within the relaxation region accelerates the first crystallization process to bcc structures.

References

[1] Suryanarayana C 1991 *Materials Science Technology* vol 15, ed R W Cahn (Weinheim: Chemie) p 57
[2] Inoue A, Ohtera K and Masumoto T 1988 *Japan. J. Appl. Phys.* **27** L736
[3] Inoue A and Masumoto T 1992 *Proc. 3rd Int. Conf. on Aluminium Alloys (Trondheim)* vol 3, ed Arneberg, O Lohne, E Nes and N Ryum p 45
[4] Inoue A 1997 *Handbook on the Physics and Chemistry of Rare Earths* vol 24, ed K A Gschneidner and L Eyring (Amsterdam: Elsevier)
[5] Dill B, Li Y, Al-Khafaji M, Rainforth W M, Buckley R A and Jones H 1994 *J. Mater. Sci.* **29** 3913
[6] Guo J Q, Kita K, Ohtera K, Nagahora J, Inoue A and Masumoto T 1994 *Mater. Lett.* **21** 279
[7] Gille W, Kabisch O and Schmidt U 1996 *Conf. Proc., The Aluminium Alloys of High Quality—Theory and Practice (Baranow, Poland)*
[8] Christian J W 1975 *The Theory of Transformation in Metals and Alloys* part 1 (Oxford: Pergamon)
[9] Schmidt U, Schmidt B, Zahra C Y and Zahra A-M 1999 *Proc. Int. Conf. on Light Alloys and Composites (Zakopane)* p 91
[10] Schmidt U and Schmidt B 2000 *J. Mater. Sci. Lett.* **19** 2183
[11] Schmidt U, Eisenschmidt C, Vieweger T, Zahra C Y and Zahra A-M 2000 *J. Non-Cryst. Solids* **271** 29
[12] Schmidt U and Schmidt B 2002 *J. Non-Cryst. Solids* at press
[13] Kissinger H E 1957 *Anal. Chem.* **29** 170
[14] Wolny J, Soltys J, Smardz L, Dubois J M and Calka A 1984 *J. Non-Cryst. Solids* **65** 40
[15] ICDD® 1997 *JCPDS—International Centre for Diffraction Data* 24-0501 and 19-0026 and 04-0787
[16] Predel B 1991 *Landolt-Börnstein New Series* vol IV/5a ed O Madelung (Berlin: Springer) p 190
[17] Rubshtein A, Rosenberg Y, Frenkel A, Manov V, Veliyulin E, Voronel A and Stern E A 1995 *Mater. Sci. Forum* **179–181** 839
[18] Faber T E and Ziman J M 1965 *Phil. Mag.* **11** 153
[19] Schmidt U, Eisenschmidt C, Zahra C Y and Zahra A-M 2001 *J. Non-Cryst. Solids* **289** 75
[20] Ben Ezra Y and Fleurov V 1999 *J. Phys.: Condens. Matter* **11** 135
[21] Massalski T E (ed) 1990 *Binary Alloy Phase Diagrams* 2nd edn (Metals Park, OH: ASM International)
[22] Edington J W 1975 *Electron Diffraction in the Electron Microscope* (Eindhoven: Philips)
[23] Kittel C 1999 *Einführung in die Festkörperphysik* (Munich: Oldenbourg)
[24] Gaskell P H 1989 *Models for the Structure of Amorphous Metals (Springer Topics in Applied Physics vol 53)* ed H Beck and H-J Güntherodt (Berlin: Springer) p 5
[25] Matsubara E, Waseda Y, Inoue A, Ohtera H and Masumoto T 1989 *Z. Naturf.* a **44** 814
[26] Frenkel A, Stern E A, Voronel A, Rubshtein A, Ben-Ezra Y and Fleurov V 1996 *Phys. Rev.* B **54** 884
[27] Gibbs M R J, Evetts J E and Leake J A 1983 *J. Mater. Sci.* **18** 278